

UC Irvine

UC Irvine Previously Published Works

Title

Dynamic model of a micro-tubular solid oxide fuel cell stack including an integrated cooling system

Permalink

<https://escholarship.org/uc/item/4rh2135s>

Authors

Hering, Martin
Brouwer, Jacob
Winkler, Wolfgang

Publication Date

2017-02-01

DOI

10.1016/j.jpowsour.2016.11.070

Peer reviewed



Dynamic model of a micro-tubular solid oxide fuel cell stack including an integrated cooling system



Martin Hering^a, Jacob Brouwer^{b,*}, Wolfgang Winkler^a

^a Hamburg University of Applied Sciences, Berliner Tor 5, 20099, Hamburg, Germany

^b National Fuel Cell Research Center, University of California, Irvine, CA, 92697, United States

HIGHLIGHTS

- Quasi three-dimensional, micro-tubular solid oxide fuel cell and stack model.
- Spatially resolved, transient thermodynamic, physical and electrical model.
- Model includes an integrated cooling system.
- Model accounts for complex geometry between cells and cooling-tubes.
- Detailed temperature based gas properties calculations.

ARTICLE INFO

Article history:

Received 28 July 2016

Received in revised form

4 November 2016

Accepted 18 November 2016

Available online 30 December 2016

Keywords:

Micro-tubular solid oxide fuel cell

MT-SOFC

Integrated cooling system

Tubular stack concept

Dynamic viscosity of helium

Thermal conductivity of helium

ABSTRACT

A novel dynamic micro-tubular solid oxide fuel cell (MT-SOFC) and stack model including an integrated cooling system is developed using a quasi three-dimensional, spatially resolved, transient thermodynamic, physical and electrochemical model that accounts for the complex geometrical relations between the cells and cooling-tubes. The modeling approach includes a simplified tubular geometry and stack design including an integrated cooling structure, detailed pressure drop and gas property calculations, the electrical and physical constraints of the stack design that determine the current, as well as control strategies for the temperature. Moreover, an advanced heat transfer balance with detailed radiative heat transfer between the cells and the integrated cooling-tubes, convective heat transfer between the gas flows and the surrounding structures and conductive heat transfer between the solid structures inside of the stack, is included. The detailed model can be used as a design basis for the novel MT-SOFC stack assembly including an integrated cooling system, as well as for the development of a dynamic system control strategy. The evaluated best-case design achieves very high electrical efficiency between around 75 and 55% in the entire power density range between 50 and 550 mW/cm² due to the novel stack design comprising an integrated cooling structure.

© 2016 Published by Elsevier B.V.

1. Introduction

In the early 1990s micro-tubular high temperature solid oxide fuel cells (MT-SOFCs) were first introduced by a research group under Professor Kevin Kendall [1]. Those cells have, in general, a diameter of no more than 10 mm and are operated in a temperature range of 500–1000 °C, which is based on the supporting structure of the cell and the used materials. MT-SOFCs can be used in a variety of applications, for instance as “auxiliary power units,

automotive power supplies, mobile electricity generators and battery re-chargers” [1]. MT-SOFCs are able to achieve high electrical efficiencies [2,3], while showing long term stability [2,4] due to enhanced thermal cycling performance with rapid start-up and shut-down capabilities [2,4–6] and high thermal shock resistance [1,5,6]. Additionally, MT-SOFCs are highly fuel flexible [1,2], including the capability to be operated in a pure internal reforming mode [1,3]. MT-SOFCs have low emissions of carbon dioxide and criteria pollutants [2] and the production processes have the potential to deliver technical solutions at low costs [4,7].

MT-SOFC technology has a wide range of possible applications and advantages that could solve worldwide energy challenges, like shortage of conventional energy resources, reduction of the

* Corresponding author.

E-mail address: jb@nfrc.uci.edu (J. Brouwer).

greenhouse gases and criteria pollutants, demand for sustainable and highly efficient electrical supply and improvement of energy efficiency.

In the current work a novel anode-supported MT-SOFC stack design with the possibility of an integrated cooling loop [2] is modeled, evaluated and analyzed. This type of MT-SOFC with integrated cooling could well be applied to hybrid SOFC-Stirling engine systems [8,9]. In the design, it is possible to internally cool the stack by thermal radiation and thus reduce the air cooling demand significantly. Therefore, the exhaust gas losses, as well as the auxiliary compressing power of the air supply are reduced. As illustrated in Fig. 1a, inside the stack, the anode of each cell is connected via a cone shaped metallic interconnect with the cathode of the adjacent cell. Several of the resulting series connections of micro-tubular cells can be arranged in a stack concept by linking the cathodes of each layer by a metallic interconnect. Therefore, the current is collected without the need for additional wiring due to the cone shaped interconnecting elements. Moreover, it is possible to integrate a cooling system by replacing a serial connected cell arrangement with a heat exchanger tube. Therefore, the heat has to be rejected by a cooling fluid inside of the heat exchanger tubes. This cooling fluid can be circulated in a closed loop if a heat sink, such as an external heat engine, is integrated in the total system setup. This integrated cooling-loop in the form of a heat exchanger is able to reject the waste heat of the stack and transfer it to an adjacent heat sink, for instance an external combustion engine, like a Stirling-engine. Thus, the stack design can be integrated into a hybrid system. In theory such a hybrid system is identical to the ideal reversible isothermal fuel cell process [2,10].

The major beneficial features of the micro-tubular design with an integrated heat exchanger are summarized below [2]:

- Small micro-tubular cell sizes and short distances to the interconnect reduce the thermal stresses
- The cones allow a sealing and an orientation of the tubes in the assembly
- Different thermal expansions of the tube and the metallic cone shaped connectors are possible without damage
- Highly flexible stack and interconnect geometries allow a wide range of applications
- Stability of the stack is increased by the metallic interconnect plates
- The interconnect plates connect the cascading MT-SOFCs in series as well as parallel on a single plate
- The cascading of multiple cells allows enhanced voltages
- Easy, compact, light and robust stack design
- High material flexibility of the interconnects and cooling-tubes
- Option for the integration of an internal heat exchanger by replacing a series of cascading cells with a cooling-tube
- Extracted heat can be used for gas preheating, fuel pre-forming or in an external heat sink (heat-engine, combined heat and power or endothermic chemical process)

In our previous work the MT-SOFC stack model was used to determine a best-case design based upon a parametric variation analysis [12]. The focus of this paper is the detailed presentation of the stack design and modeling basis, and the outline of further results of the best-case design, including the in depth evaluation of

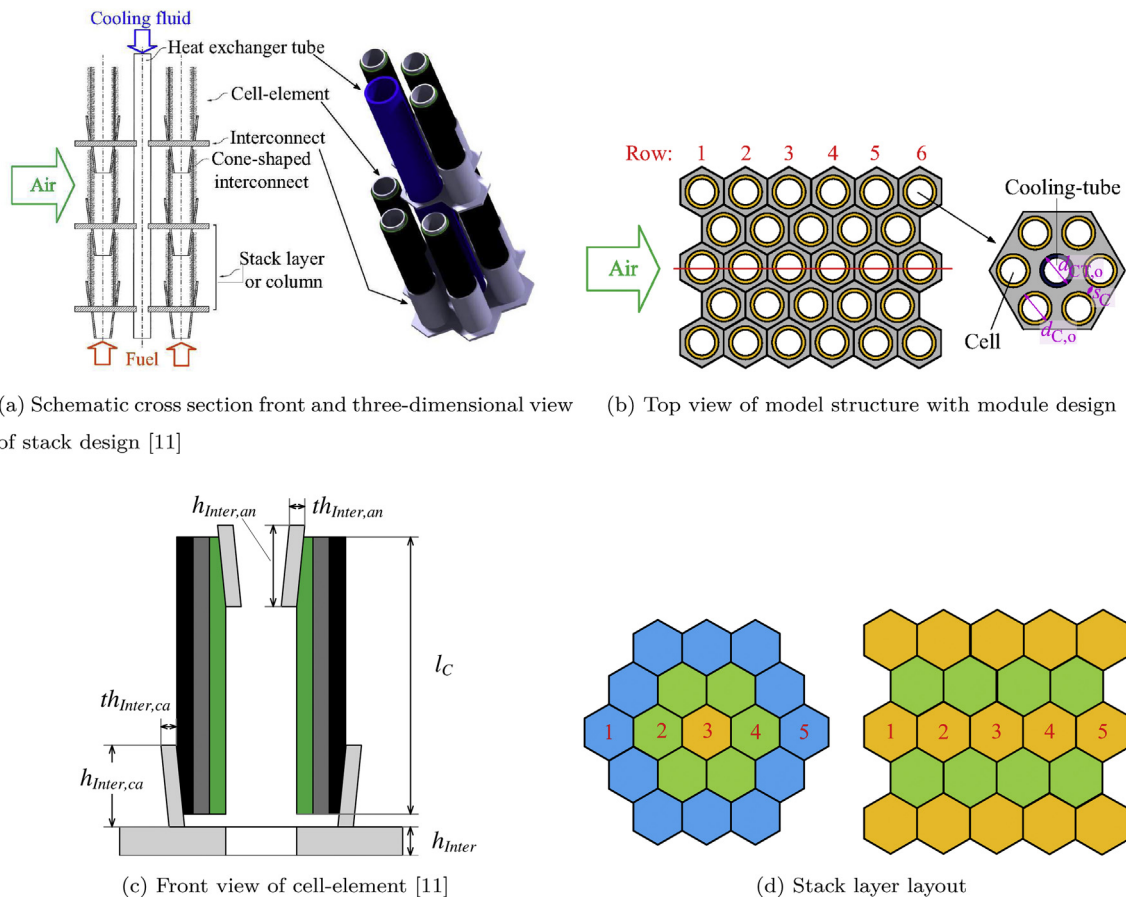


Fig. 1. Stack design and layout.

temperature, power density and fuel utilization distribution, as well as the analysis of the stack voltages and efficiency over a wide range of power densities. Additionally, the novel radiation heat transfer balance of the design is presented using a function of the pitch-to-diameter ratio between cells and cooling-tubes, derived based upon Hottel's cross-string method. Moreover, the dynamic viscosity and thermal conductivity of helium is approximated as a temperature dependent sixth-order polynomial curve fit based upon a data set of atmospheric helium.

2. Modeling approach

The modeling approach includes a simplified tubular geometry and stack design, detailed pressure drop and gas property calculations, the electrical and physical constraints of the stack design that determine the current, as well as control strategies for the temperature. Moreover, an advanced heat transfer balance with detailed radiative heat transfer between the cells and the integrated cooling-tubes, convective heat transfer between the gas flows and the surrounding structures and conductive heat transfer between the solid structures inside of the stack, is included. In the stack design, high temperature tubular fuel cells are within the view of much colder cooling-tubes. Therefore, the details of radiation heat transfer were assumed to be important to predicting the temperature distributions and resulting electrochemical performance characteristics of this type of stack design.

A quasi three-dimensional, spatially resolved, transient thermodynamic, physical and electrical micro-tubular solid oxide fuel cell and stack model including an integrated cooling system is implemented in the MatLab Simulink environment, as an extension of the planar SOFC model by McLarty et al. [13–15].

As a modeling basis the previously shown vertical cross section of the stack is used. Therefore, as illustrated in Fig. 1b, in each stack layer, modules are simulated only in a straight line, in the direction of the cross-flow air stream passing over the micro-tubular cells and cooling-tubes. The number of rows is defined by the number of modules the air stream has to pass. The governing dynamic equations are only solved for a single cell of a module, containing 6 cells and a cooling-tube, since an analogous performance is assumed for each cell in the bundle of 6 cells. Therefore, by applying these boundary conditions, the thermal interactions between the cells and the cooling-tubes can be modeled in every module without the need of an extension to an entire three-dimensional model. Moreover, it is assumed that the results of the cross section of cells are representative of a “stack unit” that is repeated symmetrically throughout the entire stack. Possible heat losses of the stack to the environment or other adjacent system components have been neglected due to the assumption of an ideal stack insulation.

2.1. Geometry

In the modeling approach simplified geometries of the cell, cooling-tube and stack layer are implemented. Regarding a cell, the spacing between the PEN-structure and the interconnect layer at the top and bottom, due to the cone shaped interconnect of the anode and the cathode, are neglected. Therefore, the effect of possible turbulence at the edges of the cells, based on the increased complexity of the air and fuel stream flows, is not considered. The influence of the interconnect at the anode and cathode is only considered with regard to the active area. Thus, the interconnect is considered to be a part of the anode or cathode and only shadowing of the active surface area is taken into account. The detailed geometry of a single cell-element is shown in Fig. 1c. Regarding a cooling-tube, the influence of the spacing elements, which reduce the thermal stresses between the cooling-tube and the

interconnect, on the flow field and the conduction heat transfer is neglected. Therefore, the structural effects on the outer and inner shape of a cell and cooling-tube are neglected. In conclusion, the inner and outer structure of a cell and cooling-tube are modeled as perfect cylinders. The total geometry of a module in the simplified stack arrangement is defined by the length and outer diameter of a single cell, the spacing between two cells, the thickness of the anode, cathode, electrolyte and cooling-tube, the height of the interconnect at the anode and cathode, as well as the height of the total interconnect layer and the spacer [11].

The diameter, as well as the length of a cooling-tube are defined in relation to the geometry of a cell to match the requirements and constraints of the stack arrangement. The length of a cell and a cooling-tube are considered to be equal. The diameter of a cooling-tube is determined based upon a relation providing that the distance between a cell and a cooling-tube is half the distance between two cells, as shown in Equation (1) and Fig. 1b.

$$d_{CT,o} = d_{C,o} + s_C \quad (1)$$

All related footprint or surface areas and volumes of the solid structures of the cells and cooling-tubes, as well as the volumes of the channels on the air, fuel and cooling fluid sides are defined based upon the determined geometrical relations. Moreover, the areas and volumes of the interconnect layer are resulting from the assumed perfect hexagonal structure of a module. To define the distances between two cells either the diameter to spacing or the pitch to diameter ratio, which are geometrically correlated, is used. The correlation used is shown in Equation (2).

$$\delta_{p/d} = 1 + \frac{1}{\delta_{d/s}} \quad \text{with} \quad \delta_{d/s} = \frac{d_{C,o}}{s_C} \quad (2)$$

2.2. Stack layer layout and power

The previously introduced modeling approach leads to a certain number of simulated cells or modules in a straight line regarding the air stream based on the designated number of rows and columns. To represent an applicable total stack design the straight line of modeled modules has to be integrated into either a shell or square stack layer design. As shown for 5 modules in a straight line in Fig. 1d, the string of modules is arranged in a continuous annular arrangement in the shell design and in a rectangular square in the square design, respectively.

The number of modules in a single stack layer in the shell and square design can be calculated based upon the number of rows, as illustrated in Equations (3) and (4).

$$N_{M,SL,Sh} = 1 + \frac{3}{4} (N_{row}^2 - 1) \quad (3)$$

$$N_{M,SL,Sq} = N_{row}^2 - \frac{N_{row}}{2} \quad (4)$$

Based on the designated stack layer layout, the total number of cells in the entire stack can be computed, as shown in Equation (5), using the number of modules in the respective design, the number of cells per module and the number of stack layers or columns.

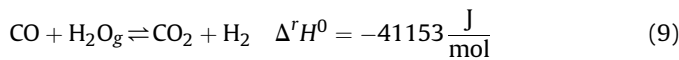
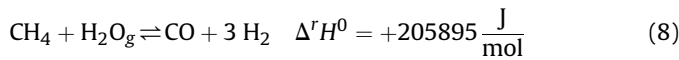
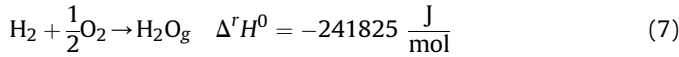
$$N_{C,S} = N_{C,M} N_{M,SL,Sh/Sq} N_{column} \quad (5)$$

Lastly, the electrical power output of the stack is defined by the total number of cells, the active surface area of the cells and the electrical areal power density as follows.

$$P_{el,S} = N_{C,S} A_{C,ac} p_A \quad (6)$$

2.3. Molar flow rates and mole fraction

In the modeling approach only the electrochemical conversion (ECC) of hydrogen and oxygen, methane steam reforming (SMR) and water gas shift (WGS) reactions are considered. The respective chemical reaction mechanisms of the ECC, SMR and WGS are illustrated in Equations (7)–(9) [10,16].



The consumed molar flow rate due to the electrochemical conversion is calculated using the stoichiometric coefficient, cell current, number of conducting electrons and Faraday constant, as shown in Equation (10) [10,16]. The subscript n indicates a node, which represents a single simulated cell.

$$\dot{n}_{Con,i,n} = \frac{\nu I_{C,n}}{N_e F} \quad (10)$$

The molar conversion flow rate of the SMR reaction can be calculated using kinetic rate constants, as shown in Equation (11). The forward (k_{SMR}^+) and backward (k_{SMR}^-) rate constant of $1.6 \cdot 10^{-7} \text{ mol m}^{-3} \text{ Pa}^{-2} \text{ s}^{-1}$ and $1.5 \cdot 10^{-20} \text{ mol m}^{-3} \text{ Pa}^{-4} \text{ s}^{-1}$ are used, respectively [17].

$$\dot{n}_{Ref,SMR,i,n} = V_{an,ac} (k_{SMR}^+ p_{CH_4,n} p_{H_2O,n} - k_{SMR}^- p_{CO,n} p_{H_2,n}^3) \quad (11)$$

The molar conversion flow rate of the water gas shift reaction can be calculated using kinetic rate constants, as shown in Equation (12). The forward (k_{WGS}^+) and backward (k_{WGS}^-) rate constants of $3.6 \cdot 10^{-7}$ and $4.3 \cdot 10^{-7} \text{ mol m}^{-3} \text{ Pa}^{-2} \text{ s}^{-1}$ are used, respectively [17–19].

$$\dot{n}_{Ref,WGS,i,n} = V_{an,ac} (k_{WGS}^+ p_{CO,n} p_{H_2O,n} - k_{WGS}^- p_{CO_2,n} p_{H_2,n}) \quad (12)$$

The change of the mole fraction of each individual species in a single node can be calculated, as shown in Equation (13), using the consumed molar flow rate due to the electrochemical conversion, the total molar flow rate at the outlet, the total molar conversion flow rate of the steam methane reforming and water gas shift reaction, as well as the resulting change in the mole fraction at the outlet, as illustrated in Equations (10) and (14)–(16). The considered species are methane, carbon monoxide, carbon dioxide, hydrogen and water vapor on the anode side, as well as oxygen and nitrogen on the cathode side [13,14].

$$\frac{dx_{i,n}}{dt} = \frac{RT}{pV_{Ch,an/ca}} (\dot{n}_{Ref,i,n} + \dot{n}_{Con,i,n} + \dot{n}_{inl,n} x_{inl,i,n} - \dot{n}_{out,n} x_{out,i,n}) \quad (13)$$

$$\dot{n}_{out,n} = \dot{n}_{inl,n} + \sum (\dot{n}_{Ref,i,n} + \dot{n}_{Con,i,n}) \quad (14)$$

$$\dot{n}_{Ref,i,n} = \dot{n}_{Ref,SMR,i,n} + \dot{n}_{Ref,WGS,i,n} \quad (15)$$

$$x_{out,i,n} = \int \frac{dx_{i,n}}{dt} \quad (16)$$

2.4. Gas properties

The enthalpy, entropy and heat capacity of methane, carbon monoxide, carbon dioxide, hydrogen, water, nitrogen, oxygen, argon and helium for a given absolute temperature and a fixed pressure level of 100 kPa are calculated using the equations and coefficients defined by McBride et al. [20].

The dynamic viscosity of each species is calculated using the equations and coefficients defined by Todd and Young [21]. However, helium is considered as a possible cooling fluid, but is not included in the published set of data by Todd and Young [21]. Therefore, following the method used by Todd and Young [21], coefficients of helium are approximated based on a sixth-order polynomial curve fit using the data set of atmospheric helium by Bich et al. [22]. The sixth-order polynomial curve fit is shown in Equation (17) and has a maximum error of 0.09% in the temperature range from 500 to 1500 K. In the illustrated equation the dynamic viscosity is calculated in 10^{-7} Pa s and τ is equal to $T/1000$. In comparison to the dynamic viscosity data of helium published by Song et al. [23] and Mehl [24] the maximum deviation is 0.40% and 0.41% in the temperature range from 500 to 1500 K, respectively.

$$\mu_{He}(\tau) = 32.73 + 689.97\tau - 596.98\tau^2 + 585.71\tau^3 - 339.96\tau^4 + 103.35\tau^5 - 12.65\tau^6 \quad (17)$$

The dynamic viscosity of a gas mixture is calculated using the method of Wilke presented by Poling et al. [25]. The calculation mechanism and the Wilke coefficient are illustrated in Equations (18) and (19), where i and j represent the species of the mixture.

$$\mu_{Mixture} = \sum_{i=1}^k \frac{x_i \mu_i}{\sum_{j=1}^k x_j \phi_{ij}} \quad (18)$$

$$\phi_{ij} = \frac{\left(1 + \sqrt{\frac{\mu_i}{\mu_j}} \sqrt{\frac{M_j}{M_i}}\right)^2}{\sqrt{8 \left(1 + \frac{M_i}{M_j}\right)}} \quad (19)$$

The thermal conductivity of each species is calculated using the equations and coefficients defined by Todd and Young [21]. As was the case for the dynamic viscosity, helium is not included in the data set. Therefore, coefficients of helium are approximated based upon a sixth-order polynomial curve fit using the data set of atmospheric helium by Bich et al. [22]. The sixth-order polynomial curve fit is shown in Equation (20) and has a maximum error of 0.10% in the temperature range from 500 to 1500 K. The thermal conductivity is calculated in $10^{-2} \text{ W m}^{-1} \text{ K}^{-1}$. In comparison to the thermal conductivity data of helium presented by Song et al. [23] and Mehl [24] the maximum deviation is 0.42% and 0.45% in the temperature range from 500 to 1500 K, respectively.

$$\kappa_{He}(\tau) = 2.58 + 53.65\tau - 45.76\tau^2 + 44.43\tau^3 - 25.61\tau^4 + 7.75\tau^5 - 095\tau^6 \quad (20)$$

The thermal conductivity of a gas mixture is calculated by the Wassiljewa equation using the Mason and Saxena modification and the relation of monatomic gases presented by Poling et al. [25]. Assuming a simplified numerical constant of 1, the thermal conductivity of a gas mixture can also be calculated using the Wilke coefficient, as shown in Equation (21).

$$\kappa_{Mixture} = \sum_{i=1}^n \frac{x_i \kappa_i}{\sum_{j=1}^n x_j \phi_{ij}} \quad (21)$$

2.5. Pressure drop

The fuel and cooling-tube are considered as perfect cylindrical pipes. Therefore, assuming ideal gas behavior to express the mean velocity, the pressure drop is calculated using the relations presented by Böswirth et al. [26], as illustrated in Equation (22).

$$\Delta p_{F/CT} = \frac{128 \mu_{F/CT} L_{C/CT} \dot{n}_{F/CT} R T_{F/CT}}{(d_{C/CT, in})^4 \pi p_{F/CT}} \quad (22)$$

Regarding the air side, the pressure drop in the air channel can be calculated analogous to the shell side of a shell and tube heat exchanger. Gaddis and Gnielinski [27] introduced a set of formulas that define the pressure drop based upon the pressure drop coefficient ξ and the number of restrictions the flow has to pass, as illustrated in Equation (23). The pressure drop coefficient is determined based upon a laminar and turbulent portion, which are dependent on the distance of the cells inside the arrangement and the Reynolds number.

$$\Delta p_{Air} = \xi N_{Restrictions} \rho_{Air} \frac{\omega_{mean, Air}^2}{2} \quad (23)$$

The number of restrictions is equal to the number of rows of cells and cooling-tubes the air stream has to pass. For the shell and square design the number of restrictions is equal and can be calculated based upon the designated number of rows in the simulation, as shown in Equation (24).

$$N_{Restrictions} = 6N_{row} - 3 \quad (24)$$

Assuming ideal gas behavior, the density and mean velocity of the air flow can be calculated. According to Gaddis and Gnielinski [27] the mean velocity is dependent upon the equivalence length of the air channel, which is defined as the length of the longest imagined string of cells and cooling-tubes orthogonal to the air stream. Therefore, the maximum number of cells and cooling-tubes on a single orthogonal row regarding the air stream is defined based upon the chosen stack layer layout. Referring to this maximum number and the spacing between the cells and cooling-tubes, the equivalence length is determined.

2.6. Heat transfer

In the modeling approach the heat transfer is simultaneously solved for every simulated module or node for every time step. For the purpose of simplification the anode, cathode and electrolyte are considered as a single positive electrode electrolyte negative electrode (PEN) element.

The conduction heat flow rates between the interconnect layers of two adjacent modules, PEN-structures of two stack layers and two adjacent cooling-tube structures are calculated using the formula of conduction heat transfer through a wall with two layers

[28]. The general formula is shown in Equation (25), in which the area and thicknesses account for the complex stack geometry. The thermal conductivities of the interconnect, the cooling-tube and PEN-structure are illustrated in Table 1. The cooling-tube is considered to be comprised of the ceramic material silicon carbide and the thermal conductivity is shown for a reference temperature of 1000 K. For the PEN-structure a value close to anode properties is chosen since the cells are anode-supported.

$$\dot{Q}_{cond, 12} = A \Delta T \left(\frac{th_1}{\kappa_1} + \frac{th_2}{\kappa_2} \right)^{-1} \quad (25)$$

The calculation of the convective heat transfer inside the fuel and cooling fluid channel is based on the assumption of a laminar flow and a constant temperature of the flow and the surrounding structure inside the node. Therefore, the set of formulas presented by von Böckh [29] can be applied to calculate the convective heat transfer inside the tubes. The general formula, using the inner tube surface area and diameter of a cell and cooling-tube, is illustrated in Equation (26). The Nusselt number is calculated using the Reynolds and Prandtl numbers, as shown in Equation (27) [28].

$$\dot{Q}_{conv, 12} = A_1 \frac{Nu \kappa}{d_{in}} (T_2 - T_1) \quad (26)$$

$$Nu = \sqrt[3]{3.66^3 + 0.7^3 + \left(1.615 \sqrt[3]{Re Pr \frac{d_{in}}{l}} - 0.7 \right)^3} \quad (27)$$

Regarding the air channel, the previously mentioned analogy to a shell and tube heat exchanger is used again. A simplified calculation mechanism of a shell and tube heat exchanger is used to estimate the convection between the air and a cell or the air and a cooling-tube [28,29]. The heat flow rate is calculated using the overflow length and surface area of a cell or cooling-tube, as illustrated in Equation (28) [29].

$$\dot{Q}_{conv, 1, Air} = A_1 \frac{Nu_{Air} \kappa_{Air}}{l_{1, over}} (T_1 - T_{Air}) \quad (28)$$

The Nusselt number is dependent upon the arrangement factor, as well as a laminar and turbulent portion, as shown in Equation (29). Both portions are related to the Reynolds and Prandtl numbers, as illustrated in Equations (30) and (31). The Reynolds number is dependent upon the mean velocity inside the shell side. The arrangement factor and the mean velocity are both dependent upon the geometrical relation between the diameter and the distance of the cells and cooling-tubes inside the arrangement. The calculation of the arrangement factor is shown in Equation (32). The mean velocity inside the air channel can be expressed using the velocity of air at the inlet of the channel and the void fraction to

Table 1

Thermal conductivity, heat capacity and density of typical interconnect, cooling-tube and PEN material [13,19,31].

Material	κ (W m ⁻¹ K ⁻¹)	c (J kg ⁻¹ K ⁻¹)	ρ (kg m ⁻³)	Reference
Interconnect	25.00	600	2000	[13]
Cooling-tube	50.00	965–1292	3200	[31]
Anode	1.86	450	3310	[19]
Cathode	5.84	470	3030	[19]
Electrolyte	2.16	430	5160	[19]
PEN	2.00	460	3300	–

account for the constraints inside the channel, as illustrated in Equations (33)–(35) [28].

$$Nu_{Air} = \left(0.3 + \sqrt{Nu_{lam}^2 + Nu_{turb}^2} \right) f_A \quad (29)$$

$$Nu_{turb} = \frac{0.037 Re_{\Psi}^{0.8} Pr}{1 + 2.443 Re_{\Psi}^{-0.1} (\sqrt[3]{Pr^2} - 1)} \quad (30)$$

$$Nu_{lam} = 0.644 \sqrt{Re_{\Psi}} \sqrt[3]{Pr} \quad (31)$$

$$f_A = 1 + \frac{4d_{C,o}}{3(d_{C,o} + s_C)} \quad (32)$$

$$\omega_{\Psi} = \frac{\omega_{Air, inl}}{\Psi} \quad (33)$$

$$\Psi = 1 - \frac{\pi d_{C,o}}{4(d_{C,o} + s_C)} \text{ for } \frac{d_{C,o} + s_C}{2d_{C,o}} \geq 1 \quad (34)$$

$$\Psi = 1 - \frac{\pi (d_{C,o})^2}{2(d_{C,o} + s_C)^2} \text{ for } \frac{d_{C,o} + s_C}{2d_{C,o}} < 1 \quad (35)$$

The convection heat transfer between the air and the interconnect layer is considered as a laminar flow along a flat plate [28,29].

Regarding the radiation heat transfer between the cells and cooling-tube in the same and to the adjacent modules, the cells and cooling-tubes are considered as gray surfaces. By neglecting the reflections of the surrounding environment and assuming equal cylindrical surface areas of all cells and cooling-tubes, the heat flow rate between two cylinders 1 and 2 can be calculated based upon the emissivities, temperature levels and view factors, as illustrated in Equation (36) [28,30].

$$\dot{Q}_{rad,12} = \frac{\sigma \epsilon_1 \epsilon_2 A_1 f_{12}}{1 - (1 - \epsilon_1)(1 - \epsilon_2) f_{12}^2} (T_1^4 - T_2^4) \quad (36)$$

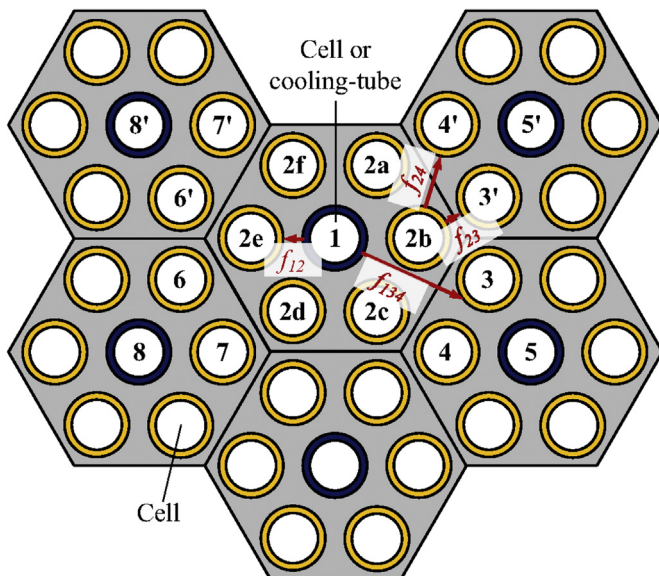


Fig. 2. Considered view factors.

Based on the assumption that modules in a vertical line on a single stack layer have an identical performance, the heat transfer in the north and south direction is neglected. As shown in Fig. 2, the radiation heat transfer in the stack arrangement can be described by only 4 different view factors since it is symmetric. Inside a module there is no radiation heat transfer between the cells since it is assumed that their temperature is identical. Therefore, only the interactions between the cells and the cooling-tube inside the same module and to the cells of the adjacent modules have to be considered. All other radiation heat transfer between the outer and central cells, for instance between 2a and 4 or 2a and 6–7', are neglected.

Cox [30] introduced the calculation of the view factors on an equilateral triangular pitch and in a hexagonal square, based upon the pitch to diameter ratio. The analogy of the design can be used to describe the view factors f_{12} , f_{23} and f_{24} . View factor f_{134} is derived following the methodology introduced by Cox [30], using Hottel's cross-string method and relating the geometry to the pitch to diameter ratio. Depending upon the pitch to diameter ratio, different types of shadowing between two cylinders can occur. Therefore, as shown in Table 2, the calculation of the view factors differs for varying pitch to diameter ratios.

According to McLarty [14], the heat generated by the electrochemical reaction in each node can be calculated using the heat of reaction, the change in the sensible enthalpy of the species and the generated electrical power, as shown in Equation (37).

$$\dot{Q}_{generated,n} = \frac{-I_n}{2F} \left(\Delta^r H_{H_2+O_2 \rightarrow H_2O}^0 + \Delta H_{H_2O} - \Delta H_{H_2} - \frac{\Delta H_{O_2}}{2} \right) - I_n E_n \quad (37)$$

In the total heat balance the heat transfer due to the ion transport of oxygen to the anode is considered, while some minor heat transfer mechanisms, for instance the conduction, convection and thermal radiation occurring at the anode and cathode interconnect, are neglected. The resulting total heat transfer balance for a single module represented by a node is shown for the individual components of the stack design and the gas flows in Table 3. The index n indicates the regarded module or node, while the indices $n+1$ and $n-1$ are used to describe the heat transfer to the adjacent nodes to the left and right or to the top and bottom.

According to McLarty [14], the change of temperature of the solid structures, the PEN, cooling-tube and interconnect, is calculated using the respective heat transfer rate, specific heat capacity, density and volume, as shown in Equation (38). Analogously, the temperature of the fluid streams, the fuel, air and cooling fluid flow, is computed based upon an overall energy balance that considers the respective heat transfer rate, sensible enthalpy at the inlet and outlet, molar heat capacity, pressure, volume of the channel, universal gas constant and temperature, as illustrated in Equation (39).

$$\frac{dT_n}{dt} = \frac{\dot{Q}_n}{\rho c V} \quad (38)$$

$$\frac{dT_n}{dt} = \frac{\dot{Q}_n + (\dot{n}H)_{in,n} - (\dot{n}H)_{out,n}}{C_{p,n} \frac{pV}{RT_n}} \quad (39)$$

The heat capacity and density of typical interconnect, cooling-tube and PEN materials are shown in Table 1. The heat capacity of the cooling-tube material, silicon carbide, is calculated as a function of the temperature, as shown in Equation (40). In Table 1 the heat capacity of silicon carbide is displayed in a temperature range from 500 to 1500 K [31].

Table 2

View factors for radiation heat transfer.

Range	Equation
$1 \leq \delta_{p/d} \leq \frac{2\sqrt{3}}{3}$	$f_{12} = \frac{1}{\pi} \left[\frac{\pi}{6} - \sqrt{(\delta_{p/d})^2 - 1} + \arctan(\sqrt{(\delta_{p/d})^2 - 1}) \right]$
$\delta_{p/d} > \frac{2\sqrt{3}}{3}$	$f_{12} = \frac{1}{\pi} \left[\sqrt{(\delta_{p/d})^2 - 1} - \arctan(\sqrt{(\delta_{p/d})^2 - 1}) - \delta_{p/d} + \frac{\pi}{2} \right]$
$1 \leq \delta_{p/d} \leq \infty$	$f_{23} = \frac{1}{\pi} \left[\sqrt{(\delta_{p/d})^2 - 1} - \arctan(\sqrt{(\delta_{p/d})^2 - 1}) - \delta_{p/d} + \frac{\pi}{2} \right]$
$1 \leq \delta_{p/d} \leq \sqrt{2}$	$f_{24} = \frac{1}{\pi} \left[\sqrt{(2\delta_{p/d})^2 - 1} - \arctan(\sqrt{(2\delta_{p/d})^2 - 1}) - 2\sqrt{(\delta_{p/d})^2 - 1} + 2\arctan(\sqrt{(\delta_{p/d})^2 - 1}) \right]$
$\delta_{p/d} > \sqrt{2}$	$f_{24} = \frac{1}{\pi} \left[\sqrt{(2\delta_{p/d})^2 - 1} - \arctan(\sqrt{(2\delta_{p/d})^2 - 1}) - \sqrt{2}\delta_{p/d} + \frac{\pi}{2} \right]$
$1 \leq \delta_{p/d} \leq \sqrt{2}$	$f_{134} = \frac{1}{2\pi} \left[2\delta_{p/d} + \arccos\left(\frac{1}{\delta_{p/d}}\right) - \sqrt{\delta_{p/d}^2 - 1} + \arccos\left(\frac{1}{\sqrt{2}\delta_{p/d}}\right) - \sqrt{2\delta_{p/d}^2 - 1} - \frac{7}{12}\pi \right]$
$\sqrt{2} \leq \delta_{p/d} < 2$	$f_{134} = \frac{\delta_{p/d}}{2\pi} (2 - \sqrt{2 + \sqrt{3}})$
$2 \leq \delta_{p/d} < 3.86$	$f_{134} = \frac{1}{\pi} \left[\sqrt{\delta_{p/d}^2 (2 + \sqrt{3}) - 1} + \arcsin\left(\frac{1}{\delta_{p/d} \sqrt{2 + \sqrt{3}}}\right) + \arccos\left(\frac{1}{\delta_{p/d}}\right) - \sqrt{\delta_{p/d}^2 - 1} - \frac{\delta_{p/d}}{2} \sqrt{2 + \sqrt{3}} - \frac{5}{12}\pi \right]$
$\delta_{p/d} \geq 3.86$	$f_{134} = \frac{1}{\pi} \left[\sqrt{\delta_{p/d}^2 (2 + \sqrt{3}) - 1} - \arctan(\sqrt{\delta_{p/d}^2 (2 + \sqrt{3}) - 1}) - \delta_{p/d} \sqrt{2 + \sqrt{3}} + \frac{\pi}{2} \right]$

Table 3

Heat transfer balance.

Element	Heat transfer balance
PEN-structure	$\dot{Q}_{PEN,n} = \pm \dot{Q}_{C,Air,conv,n} \pm \dot{Q}_{PEN,F,conv,n} \pm \dot{Q}_{PEN,cond,n+1,n-1} \pm \dot{Q}_{rad,n} + \dot{Q}_{generated,n} \pm \dot{Q}_{rad,n-1/n+1}$
Cooling-tube	$\dot{Q}_{CT,n} = \pm \dot{Q}_{CT,Air,conv,n} \pm \dot{Q}_{CT,CF,conv,n} \pm \dot{Q}_{CT,cond,n+1/n-1} \pm \dot{Q}_{rad,n}$
Cooling fluid	$\dot{Q}_{CF,n} = \pm \dot{Q}_{CT,CF,conv,n}$
Fuel	$\dot{Q}_{F,n} = \pm \dot{Q}_{Inter,F,conv,n} \pm \dot{Q}_{PEN,F,conv,n} + \dot{Q}_{Ion,transfer,n}$
Air	$\dot{Q}_{Air,n} = \pm \dot{Q}_{Inter,Air,conv,n/n-1} \pm \dot{Q}_{C,Air,conv,n} \pm \dot{Q}_{CT,Air,conv,n} - \dot{Q}_{Ion,transfer,n}$
Interconnect	$\dot{Q}_{Inter,n} = \pm \dot{Q}_{Inter,Air,conv,n/n-1} \pm \dot{Q}_{Inter,cond,n+1/n-1} \pm \dot{Q}_{PEN,cond,n} \pm \dot{Q}_{PEN,cond,n-1} \pm \dot{Q}_{Inter,F,conv,n}$

$$c_{SiC}(T) = 1267 + 0.05 T - 123 \cdot 10^6 T^{-2} + 205 \cdot 10^8 T^{-3} \quad (40)$$

2.7. Electrochemical model

The total losses at the cathode due to activation, diffusion and concentration losses can be calculated using Equation (41) [13,14].

$$\Delta E_{ca,n} = a \frac{RT_n}{4F} \ln \left[\frac{i_n p_{amb}}{i_{ex} p_{ca} \left(x_{O_2,n} - \frac{th_{ca} i_n RT_n}{4F p_{ca} D} \right)} \right] \quad (41)$$

It is assumed that the magnitude of the cathode overpotentials is much larger than those in the anode, which can be neglected since hydrogen has much higher diffusivity and reactivity than oxygen in typical SOFC material sets. Additionally, the ohmic loss can be calculated using the area specific resistance, as illustrated in Equation (42) [13,14].

$$\Delta E_{Ohmic,n} = \frac{i_n th_{PEN} T_n}{B} \exp \left(\frac{e_{act}}{RT_n} \right) \quad (42)$$

The characteristic parameters of SOFCs used in the polarization Equations (41) and (42) are shown in Table 4.

The transfer coefficient used by McLarty et al. [13] is in good accordance with other values published in literature. Cui et al. [32] and Zhu and Kee [33] are using a value of 0.5, while Leonide et al. [34] published a value of 0.65 and García-Camprubí et al. [35] is varying the parameter between 0.25 and 1.5. The exchange current density is chosen based upon the values used by Cui et al. [32],

which are in agreement with the values of 2000–2300 Am⁻² reported by García-Camprubí et al. [35]. Chung and Chung [36] reported diffusivity constants from 0.56 · 10⁻⁵ to 2.4 · 10⁻⁵ m² s⁻¹, which are in good accordance with the value used by McLarty et al. [13]. The electrolyte constant reported by McLarty [14] is matching the magnitude of the parameter published by Leonide et al. [34] of 5.8 · 10⁷ K Ω⁻¹ m⁻¹. Lastly, the electrolyte activation energy used by McLarty et al. [13] is also corresponding to the parameters reported by Zhu and Kee [33], Leonide et al. [34] and García-Camprubí et al. [35] of 8 · 10⁴, 9.2 · 10⁴ and 12 · 10⁵ J mol⁻¹, respectively.

2.8. Physical constraints and controllers

For applying the physical constraints the current per node is used as the main variable since the voltage and thus the power can be described as a function of the current. In total, the current constraint is dependent upon three individual physical constraints that are based on a conceptual feedback control of the power density, the voltage of the cells on a stack layer and the current through every stack layer. Firstly, the power density constraint is applied to vary the current to match the average cell power density to the designated power density. Secondly, in the stack design every cell on a single stack layer is electrically connected in parallel to each other cell on the same stack layer. Therefore, every cell on a specific stack layer is forced to run at an identical voltage to satisfy the equipotential surface constraint that is made for electrically connected cells in the quasi 3D-model. Thirdly, in the stack design each stack layer is electrically connected in series. Therefore, a constraint is applied to match the current of every layer to the sum of the currents of the cells on each individual layer. Each individual

Table 4
Characteristic SOFC overpotential parameters [13,14,32].

Parameter	Value	Reference
Charge transfer coefficient – a	0.7	McLarty et al. [13]
Exchange current density – i_{ex} in $A\ m^{-2}$	2000	Cui et al. [32]
Effective oxygen diffusivity – D in $m^2\ s^{-1}$	$2 \cdot 10^{-5}$	McLarty et al. [13]
Electrolyte constant – B in $K\ \Omega^{-1}\ m^{-1}$	$9 \cdot 10^7$	McLarty [14]
Electrolyte molar activation energy – e_{act} in $J\ mol^{-1}$	10^5	McLarty et al. [13]

constraint produces an error between the desired and returned (simulated measurement) state variable that is minimized simultaneously, by the variation of the current in each simulated cell, to reach a solution for each time step using a variable time-step solver in the MatLab Simulink environment.

The temperature in the stack is controlled by the cooling fluid flow rate. Therefore, a proportional integral differential (PID) controller is developed, tuned and implemented in the MatLab Simulink simulation environment to manipulate the cooling fluid flow rate at each time step based upon feedback of cell and stack temperature differences which must be maintained at a maximum limiting value. The temperature spread of an individual cell has to be controlled since the temperature distribution in a system with integrated radiative cooling can exceed the thermal shock resistance of a single cell. Therefore, the temperature spread of the entire stack and of the individual cell with the highest spread are compared and the one closest to the limit is used by the controller to determine the coolant flow rate manipulation required. The molar flow rate of fuel and air is determined by the cell current and the designated fuel and air utilization factors. Therefore, two additional PID controllers are developed, tuned and implemented in the MatLab Simulink environment to manipulate the fuel and air flow rates to match the designated utilization factors. It should be noted that the air, fuel and cooling fluid are each distributed with the help of a manifold and an individual single controller is applied per fluid, respectively.

The implementation of the physical constraints and controllers results in a stack design, that runs at a designated power density, with equal voltages of cells on a single stack layer, constant current through every stack layer, fixed air and fuel utilization factors, as well as a designated temperature level. Additionally, the applied control environment allows load following by the variation of the power density to follow any given demand.

3. Results

The operating, geometry and material properties for the evaluated best-case design, which were determined based upon a parametric variation analysis, are listed in Table 5 [12,37]. The fuel side is supplied with humidified methane.

The resulting PEN temperature distribution for a representative cross section of the stack is shown Fig. 3a. As illustrated the resulting temperature profile exhibits a cone shape with its temperature maximum in the upper central portion of the stack. At the fuel inlet most of the internal steam methane reforming is occurring. Therefore, the first column has the lowest temperature. The air, fuel and cooling fluid are heated up as they flow through the stack and the cooling effect of the methane steam reforming is vanishing since methane tends to react completely on the first columns. This results in the previously mentioned cone shaped temperature profile since the cooling fluid is streaming in a counter-flow or cross-flow regarding the fuel or air stream, respectively. Nevertheless, the occurring temperature spreads of adjacent single cells are low and therefore the temperature profile

Table 5
Operating, geometry and material properties for the evaluated design.

Parameter	Value
Power density – p_A in $mW\ cm^{-2}$	300
Type of cooling fluid	Ar
Cooling fluid flow direction	Counter-flow
Inlet fuel temperature – $T_{F,ini}$ in K	1123
Inlet air temperature – $T_{Air,ini}$ in K	1048
Inlet cooling fluid temperature – $T_{CF,ini}$ in K	973
Limiting temperature spread – ΔT in K	70
Air utilization factor	0.3
Fuel utilization factor	0.9
Steam-to-carbon-ratio	1.5
Number of columns – N_{column}	9
Number of rows – N_{row}	9
Stack layer design option	Square
Outer diameter of a cell – $d_{C,o}$ in mm	3
Cell diameter to spacing ratio – $\delta_{d/s}$	1.5
Thickness of anode in μm	200
Thickness of cathode in μm	50
Thickness of electrolyte in μm	25
Thickness of anode/cathode interconnect in mm	0.2
Length of a single cell – l_C in mm	10
Interconnect height at anode and cathode in mm	0.5
Height of interconnect layer – h_{inter} in mm	0.2
Thickness of a cooling-tube in μm	150
Height of the spacer – h_{sp} in mm	0.2
Emissivity of the cell – ϵ_C	0.4
Emissivity of the cooling-tube – ϵ_{CT}	0.4

is considered as locally uniform which reduces local thermal stresses.

In combination with the applied physical constraints, the cone shaped temperature profile leads to a non uniform current or power density distribution, as displayed in Fig. 3b. The highest power densities occur in the front central portion of the stack and result in a faster depletion of hydrogen. This effect causes the changing power density distribution in the upper portion of the stack since the hydrogen content in the first rows is too low to sustain a strong electrochemical conversion. Therefore, more hydrogen is converted in the upper middle and end portion of the stack, which is directly correlated with the higher cell currents. However, the low hydrogen content in the upper first rows of the stack leads to an enhanced formation of carbon dioxide since the water gas shift equilibrium reaction is shifting to the product side. This strong shift is based on Le Chatelier's principle as water vapor is formed and hydrogen is depleted to very low mole fractions due to the electrochemical conversion. However, analogous to the temperature distribution, the individual power density spreads between adjacent cells are low and therefore the power density distribution is also considered as locally uniform preventing hot spots and cell damage.

The described power density distribution is directly related to the fuel utilization factor per single cell distribution, as illustrated in Fig. 3c. As illustrated, the fuel utilization factor distribution has a non uniform profile with the maximum occurring in the top column or stack layer of the first row of cells. In the top left region of

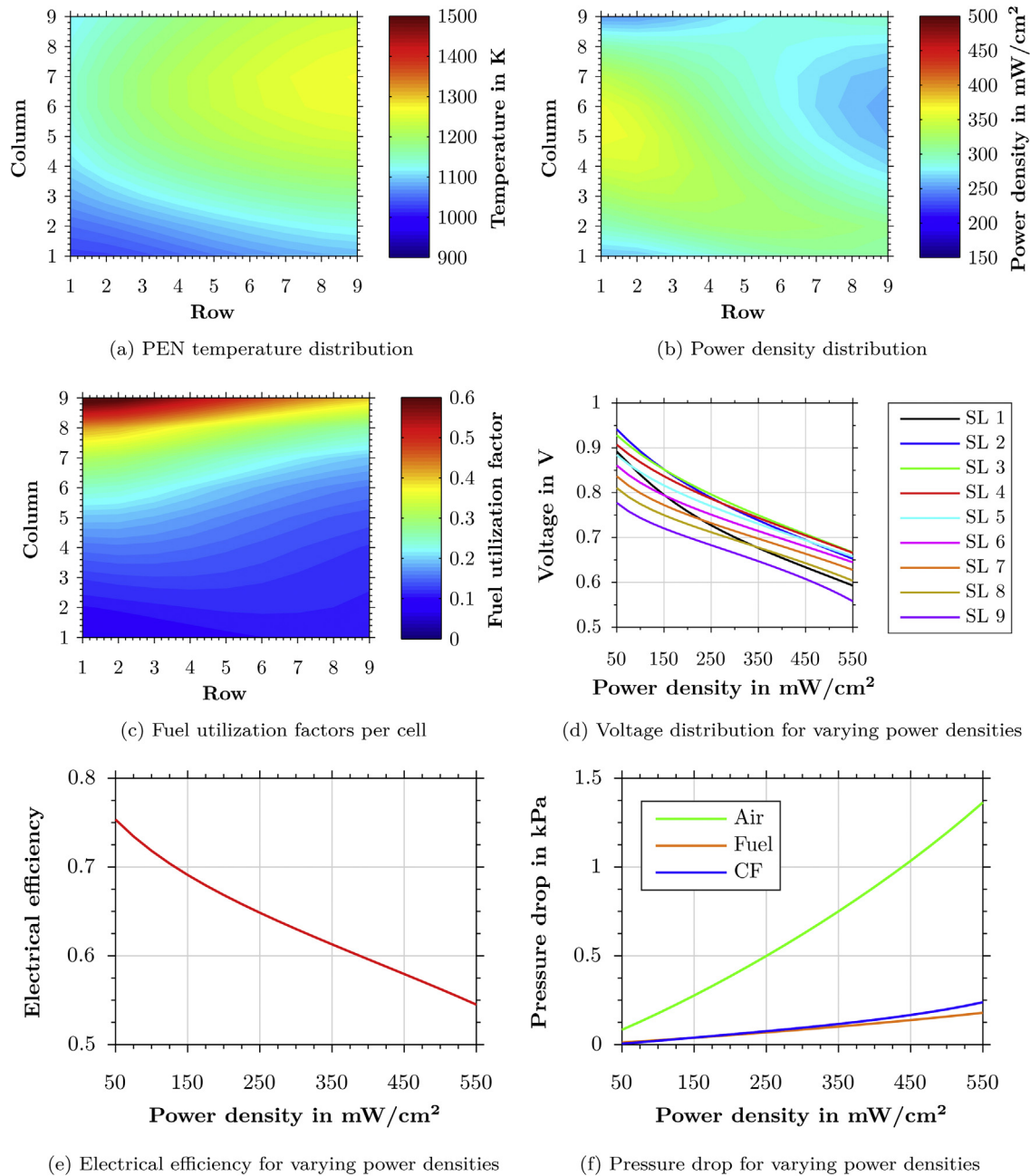


Fig. 3. Best-case design results.

the stacks cross section the fuel utilization factors of individual cells reach very high values of around 0.6. The higher fuel utilization factors in the front portion of the stack are a result of the higher power densities in the front central portion of the stack since fuel is consumed excessively. It should be noted that the applied controller guarantees a total fuel utilization factor of the stack of 0.9. However, a single row of 9 cells in series can have a higher total fuel utilization factor than 0.9, if the other rows have lower total fuel utilization factors resulting in a fuel utilization factor of the entire stack of 0.9. Therefore, a fuel utilization factor of around 0.6 at the end of a row of 9 cells in series is a very high value since the majority of the fuel is already depleted at the higher columns of the stack. As a result, the high occurring fuel utilization factors can lead to fuel starvation and irreversible cell damage. Therefore, the fuel supply needs to be accurately controlled to prevent fuel

starvation and stack damage. Additionally, the desired fuel utilization factor of the stack could be reduced to minimize the risks of stack and cell damage.

In Fig. 3d the progression of the voltage of each individual stack layer (SL) or column is shown for power densities between 50 and 550 mW/cm^2 . As illustrated, all stack layers follow a general trend with decreasing voltages for increasing power densities based upon higher losses. However, the voltage decline of stack layer or column 1 is disproportional since the majority of the methane steam reforming is occurring at the cells of the first column of the stack. Therefore, an increase of the power density leads to an enhanced supply of fuel and thus to higher cooling effects due to steam methane reforming. In sum, the ohmic losses on the first stack layer are therefore disproportionately higher due to reduced average temperatures. Therefore, even though the first stack layer has the

riches fuel supply the voltages are always lower compared to the second layer based upon increased cooling due to enhanced steam methane reforming. In Fig. 3e the efficiency of the stack is outlined for varying power densities. As illustrated, the electrical efficiency is decreasing for increasing power densities with an intermediate slope, following the trend of the average voltage. Nevertheless, the electrical efficiency is still remarkably high even for high power densities showing values between roughly 55 and 75%. The evaluated design, outlined in Table 5 with a power density of 300 mW/cm², achieves an electrical efficiency of 63% with a power output of 1.1 kW. Additionally, the very low resulting pressure drops of the stack design are illustrated in Fig. 3f for the evaluated power density range. As shown, the pressure drop of the cooling fluid (CF) and fuel is only slightly influenced by an increasing power density due to the laminar flow inside the straight pipes, whereas the pressure drop on the air side rises slightly due to the increased cooling demand that requires an increase in the air flow rate. However, even at very high power densities of 550 mW/cm² the air side pressure drop is still under 1.5 kPa, highlighting the low overall pressure drop of the design approach.

The evaluation clarifies that the chosen modeling approach with the applied physical constraints and controllers allows a detailed analysis of a micro-tubular stack design with an integrated cooling structure. The model evaluation accounts for the complex geometrical relations and achieves explainable and consistent results for a wide range of parametric variations. The results also justify the necessity of developing the sophisticated heat transfer balance to account for all thermal interactions between air, fuel and cooling-fluid, ultimately yielding the baseline to optimize the temperature distribution throughout the entire stack. Additionally, the evaluated design shows high electrical efficiency and voltages, as well as low pressure drops at the fuel, cooling fluid and air channels [12,37].

4. Conclusion

A quasi three-dimensional, spatially resolved, transient thermodynamic, physical and electrochemical micro-tubular solid oxide fuel cell and stack model including an integrated cooling system was developed. The modeling approach accounts for the complex geometrical correlations between cells and cooling-tubes that affect the heat balance and pressure drop calculations. The analogy of the stack design to a shell and tube heat exchanger was used to determine the pressure drops and convective heat transfer relations. The calculations are based upon a detailed temperature based computation of major gas properties like the dynamic viscosity and thermal conductivity of each species. A detailed radiative heat transfer balance was implemented to account for thermal interactions between the cells and cooling-tubes. Physical constraints provide that the current and voltage are calculated in accordance with the stack design electrical configuration. The temperature is controlled by a feedback control of the cooling fluid flow rate to match the cell and stack temperature spread to a designated limiting value. The evaluation based upon the chosen operating, geometry and material properties clarified that the modeling approach achieves explainable and consistent results. The evaluated design achieves an electrical efficiency of 63% with a power output of 1.1 kW running at a power density of 300 mW/cm². The model can be used to predict stack sizes and performance. Additionally, the model provides the basis for the design and development of a stack prototype for testing and validation. Meanwhile, feasible materials have to be chosen and tested to address the mechanical and sealing challenges of the proposed MT-SOFC stack design.

Acknowledgments

We gratefully acknowledge the support of Dustin Fogle McLarty, Ph.D. in the model development process.

References

- [1] V. Lawlor, S. Griesser, G. Buchinger, A. Olabi, S. Cordiner, D. Meissner, J. Power Sources 193 (2009) 387–399.
- [2] G. Tsotridis, Micro-tubular solid oxide fuel cell arrangement, 2012. US Patent App. 14/119,249.
- [3] V. Lawlor, J. Power Sources 240 (2013) 421–441.
- [4] C. Chen, M. Liu, L. Yang, M. Liu, Int. J. Hydrogen Energy 36 (2011) 5604–5610.
- [5] F. Calise, G. Restuccia, N. Sammes, J. Power Sources 195 (2010) 1163–1170.
- [6] N. Akhtar, S. Decent, D. Lohin, K. Kendall, J. Power Sources 193 (2009) 39–48.
- [7] Internal communication with Professor Dipl.-Ing. Dr.techn. Wolfgang Winkler, 2014.
- [8] N. Kamran, M. Hering, Dimensioning of an SOFC-Stirling System - Literature Research and Modeling of SOFC-Stirling Hybrids, Hamburg University of Applied Sciences, 2014.
- [9] W. Winkler, H. Lorenz, J. Power Sources 106 (2002) 338–343.
- [10] W. Winkler, Brennstoffzellenanlagen, Springer, 2002.
- [11] M. Hering, Dimensioning of an SOFC-Stirling System - Conception of the SOFC Stack, Hamburg University of Applied Sciences, 2014.
- [12] M. Hering, J. Brouwer, W. Winkler, J. Power Sources 303 (2016) 10–16.
- [13] D. McLarty, J. Brouwer, S. Samuelsen, Int. J. Hydrogen Energy 38 (2013) 7935–7946.
- [14] D.F. McLarty, Fuel Cell Gas Turbine Hybrid Design, Control, and Performance, University of California, Irvine, 2010.
- [15] D.F. McLarty, Thermodynamic Modeling and Dispatch of Distributed Energy Technologies Including Fuel Cell–Gas Turbine Hybrids, University of California, Irvine, 2013.
- [16] K. Kendall, S.C. Singhal, High Temperature Solid Oxide Fuel Cells: Fundamentals, Design and Applications, Elsevier Oxford, UK, 2003.
- [17] W. Lehnert, J. Meusinger, F. Thom, J. Power Sources 87 (2000) 57–63.
- [18] M. Ni, Int. J. Hydrogen Energy 37 (2012) 1731–1745.
- [19] N. Akhtar, S. Decent, K. Kendall, J. Power Sources 195 (2010) 7796–7807.
- [20] B.J. McBride, S. Gordon, M.A. Reno, NASA Tech. Memo. 4513 (1993).
- [21] B. Todd, J. Young, J. Power Sources 110 (2002) 186–200.
- [22] E. Bich, J. Millat, E. Vogel, J. Phys. Chem. Ref. Data 19 (1990) 1289–1305.
- [23] B. Song, X. Wang, K. Kang, Z. Liu, Cryogenics 61 (2014) 1–7.
- [24] J.B. Mehl, Comptes Rendus Phys. 10 (2009) 859–865.
- [25] B.E. Poling, J.M. Prausnitz, J.P. O'Connell, The Properties of Gases and Liquids, fifth ed., McGraw-Hill Professional, 2000.
- [26] L. Bösir, S. Bschorer, Technische Strömungslehre: Lehr- und Übungsbuch, ninth ed., Vieweg+Teubner Verlag, 2012.
- [27] E.S. Gaddis, V. Gnielinski, Chemical Engineering and Processing: Process Intensification, vol. 36, 1997, pp. 149–159.
- [28] Verein Deutscher Ingenieure, VDI Heat Atlas, second ed., Springer, 2010.
- [29] P. von Böckh, Wärmeübertragung: Grundlagen und Praxis, second ed., Springer, 2006.
- [30] R.L. Cox, Radiative Heat Transfer in Arrays of Parallel Cylinders, Oak Ridge National Laboratory, 1976.
- [31] A.H. Rashed, Properties and Characteristics of Silicon Carbide, Poco Graphite, Inc., 2002.
- [32] D. Cui, L. Liu, Y. Dong, M. Cheng, J. Power Sources 174 (2007) 246–254.
- [33] H. Zhu, R.J. Kee, J. Power Sources 117 (2003) 61–74.
- [34] A. Leonide, S. Hansmann, A. Weber, E. Ivers-Tiffée, J. Power Sources 196 (2011) 7343–7346.
- [35] M. García-Camprubí, S. Izquierdo, N. Fueyo, Renew. Sustain. Energy Rev. 33 (2014) 701–718.
- [36] C.-Y. Chung, Y.-C. Chung, J. Power Sources 154 (2006) 35–41.
- [37] M. Hering, Dimensioning of an SOFC-Stirling System - Micro-tubular SOFC-stack Evaluation, Modeling and Analysis, Hamburg University of Applied Sciences, 2014.

Nomenclature

List of Latin symbols

- \dot{n} : Molar flow rate in mol s⁻¹
 \dot{Q} : Heat flow rate in W
 $\Delta^r H^0$: Standard enthalpy of reaction in J mol⁻¹
 A : Area in m²
 a : Charge transfer coefficient
 B : Electrolyte constant in K Ω⁻¹ m⁻¹
 c : Specific heat capacity of solids in J kg⁻¹ K⁻¹
 C_p : Molar heat capacity for constant pressure in J mol⁻¹ K⁻¹
 D : Effective oxygen diffusivity in m² s⁻¹

d: Diameter in m
E: Voltage in V
e: Electrolyte molar activation energy in J mol⁻¹
F: Faraday constant in C mol⁻¹
f: View factor
f_A: Arrangement factor
H: Enthalpy in J mol⁻¹
h: Height
I: Current in A
i: Current density in A m⁻²
k_{SMR}⁺: Velocity constant of steam methane reforming reaction (forward) in mol m⁻³ Pa⁻² s⁻¹
k_{SMR}⁻: Velocity constant of steam methane reforming reaction (backward) in mol m⁻³ Pa⁻⁴ s⁻¹
k_{WGS}⁺: Velocity constant of water gas shift reaction (forward) in mol m⁻³ Pa⁻² s⁻¹
k_{WGS}⁻: Velocity constant of water gas shift reaction (backward) in mol m⁻³ Pa⁻² s⁻¹
l: Length in m
M: Molar mass in g mol⁻¹
N: Number
Nu: Nusselt number
P: Power in W
p: Pressure in Pa
p_A: Areal electrical power density in W m⁻²
Pr: Prandtl number
R: Universal gas constant in J mol⁻¹ K⁻¹
Re: Reynolds number
s: Spacing in m
T: Thermodynamic temperature in K
t: Time in s
th: Thickness in m
V: Volume in m³
x: Mole fraction in mol mol⁻¹

List of Greek symbols

δ: Ratio
κ: Thermal conductivity in W m⁻¹ K⁻¹
μ: Dynamic viscosity in Pa s
ν: Stoichiometric coefficient of a single component
ω: Velocity in m s⁻¹
φ: Wilke coefficient
π: Pi
Ψ: Void fraction
ρ: Density in kg m⁻³
σ: Stefan Boltzmann constant in W m⁻² K⁻⁴
τ: Temperature coefficient
Δ: Change of quantity
ε: Emissivity
ξ: Pressure drop coefficient

List of subscripts

Ψ: Void fraction
ac: Active
act: Activation
amb: Ambient
an: Anode
C: Cell

ca: Cathode
CF: Cooling fluid
Ch: Channel
CH₄: Methane
CO: Carbon monoxide
CO₂: Carbon dioxide
Con: Consume
cond: Conduction
conv: Convection
CT: Cooling-tube
d/s: Diameter to spacing
e: Electron
el: Electric
ex: Exchange
F: Fuel
g: Gaseous
H₂: Hydrogen
H₂O: Water
He: Helium
i: Running index of species
in: Inner
inl: Inlet
Inter: Interconnect
j: Species
lam: Laminar
M: Module
n: Running index of nodes
n + 1: Adjacent node to the right or on top
n - 1: Adjacent node to the left or below
o: Outer
O₂: Oxygen
out: Outlet
over: Overflow
P/d: Pitch to diameter
PEN: Positive electrode electrolyte negative electrode
rad: Radiation
Ref: Reform
S: Stack
Sh: Shell layout
SiC: Silicon carbide
SL: Stack layer
SMR: Steam methane reforming reaction
Sp: Spacer
Sq: Square layout
turb: Turbulent
WGS: Water gas shift reaction

List of abbreviations

CF: Cooling fluid
ECC: Electrochemical conversion
MT: Micro-tubular
PEN: Positive electrode electrolyte negative electrode
PID: Proportional integral differential controller
SL: Stack layer
SMR: Steam methane reforming
SOFC: Solid oxide fuel cell
WGS: Water gas shift